Applied Thermal Engineering 257 (2024) 124193

Contents lists available at ScienceDirect

Applied Thermal Engineering

journal homepage: www.elsevier.com/locate/apthermeng

Research Paper

Generation of compressed air by overdriven free-displacer thermocompressors – Experimental investigation of a three-stage cascade

Fabian Fischer, Hans-Detlev Kühl *

Technische Universität Dortmund, Lehrstuhl für Thermodynamik (BCI), Emil-Figge-Straße 70 44227, Dortmund, Germany

ARTICLE INFO

Keywords:
Reciprocating thermocompressor
Multi-stage design
Compressed air
Waste heat utilization
Overdriven mode

ABSTRACT

Due to their straightforward design and advantageous operational characteristics, cascaded arrangements of overdriven free-displacer thermocompressors may provide a simple, expedient and cost-effective solution to reduce the high primary energy requirements for compressed air generation, which is a common challenge in industry. Following first experiments with a single-stage prototype, this contribution presents the first experimental realization of a three-stage cascade so that the overall concept has now been demonstrated to be fully operational for the first time. In particular, the predicted self-control capabilities of a stage located within the cascade and thus without any preset inlet or outlet pressure could be proven, whereas this had been impossible with the single-stage prototype before. Stable operation with all stages running is possible at total pressure ratios ranging from a practical maximum near 2.1 down to approximately 1.36. At even lower values, the pressure ratio of the first stage undercuts an analytically predicted lower stability limit and eventually stops, whereas the power density of the remaining stages is increased. To exploit the potential for improvement identified during the single-stage experiments, the design of the new stages is based on the first prototype, but has been optimized by a similarity-based scaling procedure and design evolution, resulting in a significant increase in power density from 7.1 W to 12.5 W per liter of displacement. To further demonstrate the capability of such a cascade to extract waste heat from a hot stream, the heater temperatures of the stages were successively reduced along the cascade by an adequate control, thus emulating a finite heat capacity rate of the stream. Although the exergy transferred to the compressed air flow is reduced in this case, the overall performance is not adversely affected. The combination of the models and the scaling approach, which have now been demonstrated experimentally, provides a comprehensive toolbox for the future development of a series machine.

1. Introduction

Compressed air is a widely used versatile industrial energy source, but its generation is relatively inefficient, resulting in elevated costs and environmental harm [1]. According to a recent survey [2], approximately 9 % of the respondent companies reported that the biggest savings were achieved by efficiency measures related to their compressed air systems. At the same time, significant amounts of waste heat at various temperature levels are either entirely unexploited or, at best, employed for low-value space heating [3–6]. 7 % of the respondents mentioned waste heat recovery as the most promising approach to improve energy efficiency [2]. This clearly reflects the growing awareness of this untapped potential. Moreover, it is foreseeable that industrial companies will be legally obliged to utilize their waste heat. As a preliminary step, German companies with a total energy consumption above 2.5 GW hours per year will be obliged to offer their waste heat potential on a public platform starting in 2025 [7]. Against this background, innovative, simple, and cost-effective solutions for waste heat utilization are of great interest.

For almost a century, reciprocating thermocompressors – which essentially correspond to the displacer system of a β- or γ-Stirling engine – have been known as a means to directly utilize heat for the compression of gases without any detour via mechanical power. However, they were only exploited for niche applications in the past, where a single compression stage was sufficient. According to the more profound literature reviews provided in [8,9], and [10], several authors developed both analytical [11–15] and numerical [8,16–18] models for the thermocompressor cycle at various levels of complexity, but only few experimental stages have been realized so far [19–22], which all feature crank-coupled displacers with an auxiliary drive. Generation of compressed air at industrial pressure levels by a cascade of individually

* Corresponding author.
E-mail address: hans-detlev.kuehl@tu-dortmund.de (H.-D. Kühl).

https://doi.org/10.1016/j.applthermaleng.2024.124193
Received 4 March 2024; Received in revised form 5 August 2024; Accepted 14 August 2024
Available online 15 August 2024

Nomenclature

Latin Letters

A	Cross-sectional area, m^2
B	Sum of the temperature-related mean volumes, m^3/K
C	Spring stiffness, N/m
c_p	Isobaric heat capacity, J kg^{-1} K^{-1}
d	Diameter, m
D	Sum of the temperature-related volume amplitudes, m^3/K
E	Exergy, J
F	Constant factor, kg s^{-1} Pa^{-2}
g	Relative change of the exergy flow, –
h	Specific Enthalpy, J kg^{-1}
j	Viscous friction coefficient, N s/m
l	Length, m
m	Mass, kg
n	Number
N	Frequency, Hz
p	Pressure, Pa
P	Power, W
Q	Heat, J
R	Specific gas constant, J kg^{-1} K^{-1}
s	Wall thickness, m
T	Temperature, K
t	Time, s
V	Volume, m^3
v	Velocity, m/s
W	Work, J
x	Position, m

Greek Letters

α	Heat transfer coefficient, W m^{-2} K^{-1}
δ	Damping constant, –
Δ	Difference
η	Efficiency, –
θ	Temperature ratio, –
λ	Thermal conductivity, W m^{-1} K^{-1}
Π	Pressure ratio, –
ρ	Ratio of cross-sectional areas of displacer and rod, –
σ	Dimensionless temperature-related dead volume, –
ψ	Scaling factor, –

Dimensionless Numbers

Nu	Nusselt number
NTU	Number of Transfer Units
Re	Reynolds number

Subscripts

0,K2	Critical lower (theoretical) stability limit
av	Avoidable
b	Bushing
C	Cylinder
c	Cold
cond	Conduction
conv	Convection
D	Displacer
h	Hot
i	Component number
in	Inlet
k	Stage number
lam	Laminar
lim	Limit (practical)
lsl	Critical lower (practical) stability limit
max	Maximum (theoretical)
opt	Optimum operating point
out	Outlet
R	Rod
r	Regenerator
rad	Radiation
tot	Total

Superscripts

$\dot{}$	Time derivative
$\bar{}$	Mean
$\hat{}$	Amplitude
$'$	Scaled quantity

designed stages was not seriously considered for reasons of complexity and cost. As a step towards economic competitiveness of such systems, Thomas and Barth [23] proposed a cascade of identical stages that may be produced at a larger scale and thus at reduced cost, but no experimental realization has been reported so far. The stages are also devised to be coupled to a common crank mechanism requiring auxiliary mechanical power, and the synchronization prevents an optimum operation of all stages in this concept. Fischer and Kühl [9] therefore suggested to omit the crank mechanism, which causes additional cost, wear and friction losses, and to provide self-sustaining overdriven free displacers instead, which may adapt their frequencies according to the operating conditions and do not require any auxiliary drive, thus further simplifying the design and reducing the manufacturing cost in an anticipated series production considerably.

Experiments with a first single-stage prototype of such an overdriven free-displacer thermocompressor have demonstrated the expected favorable operating characteristics for various inlet pressures, including the self-sustainment and self-regulation characteristics [24]. However, the power density of the prototype was 7.1 W exergy gain of the compressed air flow per liter of displacement only. This is due to the rather large cylinder diameter, which was to some extent chosen based on the availability of suitable raw stock and manufacturing limitations in the university machine shops. Since the simplified constructional concept of replacing the heat exchangers and the regenerator by a plain annular gap around the displacer proved to be fully operational and shall therefore be maintained in future designs, it was meanwhile subject to a dimensional analysis revealing that the power density scales inversely with the geometric dimensions. As the basic idea is to minimize the cost of a single unit by a large-scale series production, there appears to be some scope for an economic optimization by downsizing via a similarity-based scaling procedure.

The experimentally observed power density of the prototype was even below the theoretical predictions due to increased friction and substantial leakage losses via the guide bushings of the displacer rod. In this context, the water lubrication of these bushings, which had initially been devised to make beneficial use of the inevitable condensation of air moisture in the upper stages of a cascade, proved to be impractical, since the need to use a water-resistant polymer material for the bushings entailed severe tolerance issues. So, a different design of these bushings is needed to provide both a reliable low-friction guidance and a good sealing. Otherwise, leakage losses will substantially impair the performance particularly in the upper stages of a cascade due to the higher density of the compressed air and the larger absolute pressure differences.

Furthermore, the ability of the single stages in a cascade to adapt their operating frequency depending on the inlet and outlet pressure also implies that they may temporarily convey different mass flows. In this case, the pressures in the buffer volumes between the stages will change,

and these are in turn the inlet and outlet pressures of the stages and thus affect their frequencies again. This complex feedback mechanism, which may basically cause instability problems, has so far only been analyzed theoretically by analytical models and simulations with a third-order model implemented in MATLAB/Simulink [25]. Although stable operation could thus be confirmed within a wide range of the overall pressure ratio particularly including the practically relevant operating conditions, an experimental validation is still pending, as this was not possible by operating just a single prototype thermocompressor stage of course, but requires the realization and experimental analysis of at least a small cascade consisting of a minimum of three stages. This will also allow an experimental investigation of the theoretically predicted self-starting capabilities as well as the effect of decreasing heater temperatures along the cascade, which will typically occur when waste heat is gradually extracted from a hot stream at a gliding temperature.

Summarizing, the open issues to be addressed in this contribution therefore are the following:

- The power density of the first prototype design is so low that particularly leakage losses at the bushings cause a substantial performance degradation. Therefore, it should be increased by downsizing the single stage design according to a similarity-based scaling procedure, simultaneously maintaining the intrinsic heat transfer and viscous flow losses of the cycle at a constant level.
- The water-lubricated polymer bushings simultaneously guiding and sealing the displacer rod in the prototype design caused severe tolerance problems. Therefore, different design concepts, such as dry-running bushings made from sintered bearing bronze, need to be devised and experimentally explored in order to decrease the leakage losses substantially, particularly at elevated operating pressures.
- The proposed concept of a cascade of identical overdriven free-displacer thermocompressors has never been realized so far. It implies several open issues regarding its dynamic operating characteristics, such as the self-starting capabilities or potential instabilities due to fluctuating operating frequencies of the single stages. The related theoretical model predictions are all based on simplifying assumptions and therefore require a practical validation. This is only possible by the realization and investigation of a first experimental thermocompressor cascade, which will be reported in the following.
- Since waste heat is typically absorbed from a hot stream, such as a flue gas flow, which is gradually cooled down depending on its heat capacity, the stages are exposed to variable heater temperatures, which are in turn also affected by the operating conditions, i. e. by the heat flows absorbed by the single stages. This is another feedback effect that needs to be analyzed using the experimental cascade.
- Before manufacturing several identical stages, their design should of course be optimized, particularly regarding its reliability and constructional simplicity. To demonstrate the potential for a future low-cost series production, the number of components should therefore be further reduced, and their design should be adapted for efficient mass fabrication techniques such as deep drawing, spinning or extrusion.

2. Similarity-based scaling procedure

Fig. 1 shows a schematic drawing of the first single-stage prototype that serves as the basis for the scaling procedure. It includes all the relevant components needed to briefly explain the thermodynamic cycle. When the displacer moves downwards, the air, which acts as both the working gas and the product stream, is relocated from the cold to the hot cylinder volume via the annular gap forming the cooler, the regenerator, and the heater. Therefore, the cycle pressure increases, until the outlet valves in the displacer base open and the air is conveyed into the outlet buffer through the hollow displacer rod. When reaching the lower end of stroke, it hits the limit stop springs, reverses its direction of motion and relocates the air back from the hot to the cold

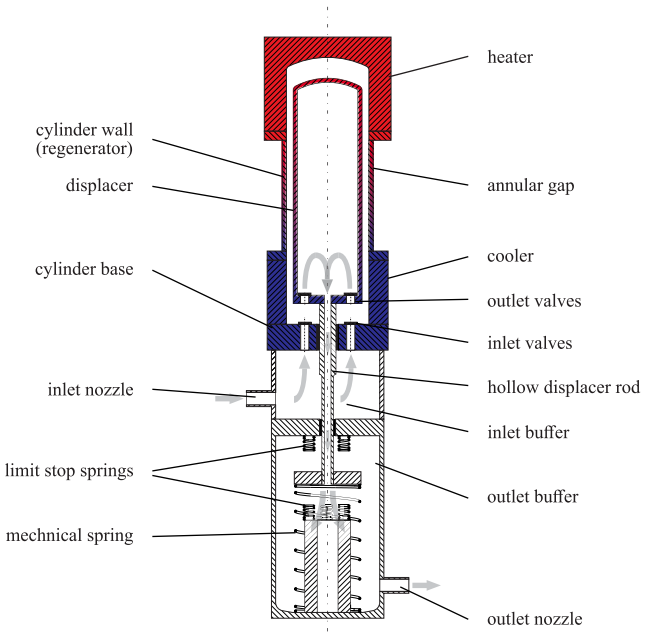

Fig. 1. Schematic drawing of the prototype of the thermocompressor with overdriven free-displacer and annular gap (following [24]).

cylinder volume. So, the pressure decreases, until the inlet pressure is undercut and the inlet valves in the cylinder base open, feeding air from the inlet buffer into the cylinder. To ensure accelerating forces during the entire cycle, the original concept included a gas spring featuring half the (negative) spring constant of the cycle [9], but the experiments demonstrated that a mechanical spring featuring a similar spring constant is sufficient. Such a spring is anyway needed to balance the weight of the displacer and to suspend it at a medium position during standstill. The experimental results [26] were used to validate a second-order numerical model [24], which is based on the isothermal model [9], but was extended by several loss mechanisms such as heat transfer limitations, fluid friction, and inlet and outlet pressure losses. In addition, gas leakage through the gaps between the displacer rod and the bushings turned out to reduce the conveyed mass flow and the practical upper limit of the pressure ratio significantly. Therefore, these leakages are also included in the model assuming laminar flow through the bushing gaps.

Despite its simplified design substituting the heat exchangers and the regenerator by a plain annular gap around the displacer, the single-stage prototype showed principally good results and proved the general feasibility of the design [24]. Therefore, a three-stage cascade could have been realized by manufacturing two more identical stages. However, potential for further improvement was identified in the design of several components, a reduction of the machining effort and an optimization of the performance by increasing the power density. Therefore, it was decided to revise the design and to build three new machines. As the machining of the parts is essentially confined to metal-cutting techniques, the machining effort for the individual stages is most easily decreased by reducing the geometrical dimensions. However, to preserve the advantageous operating behavior of the single-stage prototype, thermodynamic similarity had to be maintained. For this reason, the following quantities were kept constant:

(1) regenerator efficiency η_r
(2) ratio between required power due to flow pressure losses and absorbed heat flow
(3) ratio between dead volume and volume amplitude
(4) ratio between conduction losses and absorbed heat flow

The regenerator efficiency essentially depends on heat transfer limitations and may be evaluated as

$$\eta_r = 1/(1 + 2/NTU) \tag{1}$$

according to Urieli and Berchowitz[27], and therefore only depends on the number of transfer units,

$$NTU = \frac{\alpha A_r}{\dot{m}_r c_p} \tag{2}$$

Here, α denotes the heat transfer coefficient in the annular gap acting as the regenerator. Accordingly, $A_r \approx 2\pi d_C l_D$ denotes the overall regenerator surface area, assuming that the cylinder diameter d_C approximately applies to the displacer, too, and that the length l_D of the latter also determines the cylinder surface. $\dot{m}_r$ designates the mass flow through the gap, and c_p the isobaric heat capacity of air. As laminar flow in the gap of width s_{gap} may be assumed, the Nusselt number $Nu_{lam} = 2\, s_{gap}\, \alpha/\lambda$ is constant. Applying this and replacing $\dot{m}_r$ by the product of the density ρ and the average volume flow $\dot{V} = \pi\, d_C^2\, \hat{x}\, N$ of the air, which in turn depends on the frequency N and the stroke amplitude $\hat{x}$, Eq. (2) can be rewritten as

$$NTU = \frac{Nu_{lam}\,\lambda}{2\, s_{gap}} \frac{2\,\pi\, d_C\, l_D}{\rho\ \pi\, d_C^2\, \hat{x}\, N\, c_p} = \underbrace{Nu_{lam}\frac{\lambda}{\rho\, c_p}}_{const.} \frac{l_D}{s_{gap}\, \hat{x}\, d_c\, N} \overset{!}{=} const. \tag{3}$$

Here, a sawtooth function is assumed, so that the absolute value of the displacer velocity is constant throughout the cycle. The same applies to the mass flows. This assumption is based on the analytical results for the displacer motion presented in [9], which were confirmed by experiments with the first single-stage prototype [24]. The properties of air, such as the thermal conductivity λ, the density ρ and the isobaric heat capacity c_p, remain constant. Eq. (3) must be constant to fulfill the above condition (1). Based on the isothermal model presented by Fischer and Kühl [9], the ratio between the required power due to flow pressure losses and the absorbed heat flow is evaluated assuming laminar gap flow. In addition to the introduced geometrical quantities, it is a function of the maximum pressure ratio Π_{max}, the pressure ratio Π at the given operating point, the dynamic viscosity η, the inlet pressure p_0 and the displacer length l_D:

$$\frac{P_{\Delta p}}{\dot{Q}_h} = \frac{\frac{12\ \eta\ 4\ \widehat{V}\ N\ l_D}{\pi\ d_C\ s_{gap}^3}\, 4N\widehat{V}}{N\ p_0\ 2\ \widehat{V} \underbrace{\frac{\Pi_{max} - \Pi}{\Pi_{max} - 1} \ln\Pi}_{K}} = \underbrace{\frac{24}{K}\frac{\eta}{p_0}}_{=const.} \frac{\hat{x}\ d_C\ N\ l_D}{{s_{gap}}^3} \overset{!}{=} const. \tag{4}$$

Again, all quantities except the geometrical ones and the frequency are not affected by the scaling and remain constant. The ratio of the dead volume V_d and the volume amplitude $\widehat{V} = \pi/4 d_C^2 \hat{x}$ is evaluated as a function of the aforementioned geometrical quantities:

$$\frac{V_d}{\widehat{V}} = \frac{\pi\ d_C\ s_{gap}\ l_D}{\frac{\pi}{4}\ d_C^2\ \hat{x}} = \frac{4\ s_{gap}\ l_D}{d_C \hat{x}} \overset{!}{=} const. \tag{5}$$

The ratio between the conduction losses and the absorbed heat flow results in a function of the thermal conductivity of steel λ_{st}, the temperature difference between the heater and the cooler, the thickness of the cylinder wall s_C and the already introduced quantities:

$$\frac{\dot{Q}_{cond,C}}{\dot{Q}_h} = \frac{2\ \lambda_{st}\ \pi\ d_C\ s_C(T_h - T_c)}{l_D\ N\ p_0\ 2\ \widehat{V}\ \frac{\Pi_{max}-\Pi}{\Pi_{max}-1}\ \ln\Pi} = \underbrace{\frac{4\ \lambda_{st}\ (T_h - T_c)}{p_0\ K}}_{const.} \frac{s_C}{l_D\ \hat{x}\ d_C\ N} \overset{!}{=} const. \tag{6}$$

Substituting the product $\hat{x}\ d_C\ N$ in Eq. (4) by inserting Eq. (3) yields

$$\frac{\eta\,\lambda}{p_0\,\rho\,c_p} \frac{Nu_{lam}}{NTU} \frac{l_D^2}{s_{gap}^4} = const. \tag{7}$$

Introducing a scaling factor ψ primarily for the gap width, i.e. assuming that the scaled gap width is equal to $s'_{gap} = \psi s_{gap}$, Eq. (7) is fulfilled for a scaled displacer length $l'_D = \psi^2 l_D$, provided that NTU is constant as required. On this basis, Eq. (5) yields

$$(d_C\, \hat{x})' = \psi^3\, d_C\, \hat{x} \tag{8}$$

Inserting these results into Eq. (3), the frequency of the scaled machine is found to be

$$N' = \frac{1}{\psi^2} N \tag{9}$$

Considering Eq. (8), a further specification of the distribution of ψ^3 over the length and the diameter is necessary. In order to preserve the conditions in the annular gap, it was decided to maintain the ratio of stroke and displacer length constant, resulting in the additional conditions $\hat{x}' = \psi^2 \hat{x}$ and $d'_C = \psi d_C$. Thus, Eqs. (3), (4), and (5) are fulfilled as well. According to Eq. (9), the frequency of the single stages increases for $\psi < 1$. This is advantageous, as their power density in terms of the ratio of the exergy gain of the compressed air flow $\Delta\dot{E} = N\Delta E$ and the volume amplitude is increased:

$$\left(\frac{\dot{Q}_h}{\widehat{V}}\right)' \sim \left(\frac{\Delta\dot{E}}{\widehat{V}}\right)' = \frac{1}{\psi^2}\frac{\Delta\dot{E}}{\widehat{V}} \tag{10}$$

Introducing a constant ambient temperature T_{amb} and the specific gas constant R, the exergy gain ΔE of the compressed air per cycle may be evaluated as

$$\Delta E = \Delta m\, R\, T_{amb} \ln\Pi \tag{11}$$

In addition, the motion of the displacer approaches the desired triangular function even though the displacer mass is reduced due to a downscaling, since the dimensionless damping constant δ introduced by Fischer and Kühl [9] is not affected by the scaling.

Solely Eq. (6) cannot be fulfilled, if the wall thickness s_C of the original machine is assumed to be minimum according to Barlow's formula, since the scaled value is $s'_C = \psi^3 s_C$, whereas s_C can only be reduced linearly by the factor ψ to maintain the required strength. Table 1 summarizes the scaling factors for all relevant geometrical parameters, and Table 2 the resulting scaled operating data.

3. Experimental machine and test stand

3.1. Setup

Compared to the first single-stage prototype [24], the design of the stages of the cascade shown in Fig. 2 was significantly simplified by reducing the number of parts, bolted connections, and sealing surfaces to point out further perspectives for the conception of a low-cost series machine. The concentric design, which had been proposed for similar

Table 1
Scaling of relevant geometrical parameters.

Quantity	Symbol	Scaling factor
Max. stroke amplitude	$\hat{x}$	ψ^2
Displacer diameter	d_D	ψ
Displacer wall thickness	s_D	ψ
Displacer length	l_D	ψ^2
Annular gap width	s_{gap}	ψ
Cylinder wall thickness	s_C	ψ
Cooler length	l_c	ψ^2
Heater length	l_h	ψ^2
Displacer rod diameter 1	$d_{r,1}$	ψ
Displacer rod diameter 2	$d_{r,2}$	ψ
Length of bushing 1	l_{b1}	ψ^2
Length of bushing 2	l_{b2}	ψ^2

Table 2
Scaling of characteristic operating data.

Quantity	Symbol	Scaling factor
Volume amplitude	$\widehat{V}$	ψ^4
Absorbed heat	Q_h	ψ^4
Exergy gain of compressed air per cycle	ΔE	ψ^4
Mass conveyed per cycle	Δm	ψ^4
Frequency	N	ψ^{-2}
Exergy gain of compressed air flow	$\Delta\dot{E}$	ψ^2
Mass flow	$\dot{m}$	ψ^2

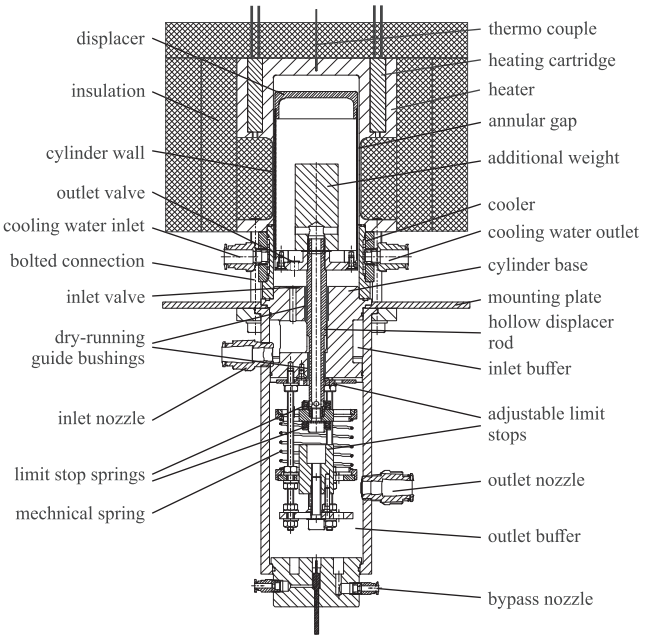

Fig. 2. Sketch of a single stage.

applications [8,16,20,28,29], had proven itself in the single-stage experiments and was therefore preserved. Here, the annular gap between the cylinder and the displacer fulfills the function of the heat exchangers and the regenerator. A major modification was implemented by combining the heater section and the regenerator to one part made of stainless steel. For a series machine, this part may be replaced by a deep-drawn cylinder equipped with additional circumferential fins. However, such techniques were not an option for an experimental machine. So, the part was machined from the solid, and the realizable minimum wall thickness therefore was $s_C = 1.2$mm. The cooler consists of an inner aluminum cylinder, which is inserted into an outer cylinder to form circumferential cooling channels. These components are mounted on the cylinder base, which includes the inlet valves and the two dry-running bushings made of bearing bronze. The cylinder base is inserted in a central square mounting plate, so that the active cycle volume is above this plate. The buffers are formed by a tube that is pushed over the cylinder base from below. As shown in Fig. 2, only one bolted joint connecting the flanges of the cylinder and the buffer wall is required to fix the assembly. The outlet buffer space accommodates the adjustable elastic limit stops as well as the mechanical spring suspending the displacer, as suggested by Fischer et al. [25].

The outlet valves are placed in the bottom of the displacer to maximize the number of valves and the cross-sectional area, respectively. The air flows through the hollow displacer rod into the outlet buffer. All valves are implemented as silicon reed valves similar to those in the prototype. To ensure an approximate center position at standstill, the total displacer mass was matched to the preload force of the mechanical spring by an additional weight. As explicated in section 2, the spring constant must be adapted to the cycle spring constant. It is $C_S = 0.105$ N/mm, which is slightly less than half the absolute value of the calculated cycle spring constant of the first stage.

The similarity-based scaling procedure introduced in section 2 was applied to determine the geometric dimensions of the stages for the cascade presented in this contribution. Given that the primary motivation for the scaling was to increase the power density, a reduced size of the new machine compared to the single-stage prototype [24] was required according to Eq. (10). A scaling factor $\psi = 0.71$, corresponding to doubling the power density, was chosen, since it constitutes a significant and substantial scaling step and is large enough to validate the scaling procedure. This scaling factor was found to yield a convenient size regarding experimental handling, component machining and assembly, particularly considering that standard components, such as bolts, are not arbitrarily scalable. Furthermore, the manufacture of the valves and the hollow displacer rod becomes more complex if the size is further reduced. It is also important to consider the entailed scaling of manufacturing tolerances in this context.

To verify the similarity-based scaling in terms of operating characteristics, Fig. 3 shows computational results obtained by the model, which is briefly introduced in section 2 and had been validated by the single-stage experiments before [24]. Since leakage and further increased friction losses are not considered in the scaling, these effects are excluded in the calculations shown in Fig. 3 for better comparability. The comparisons of the exergy transferred to the compressed air per cycle and the conveyed mass almost show the expected reduction by a factor of $\psi^4 = 0.25$. The model includes limited heat transfer in the externally heated and cooled components, as well as additional flow losses [24], such as outflow losses from the annular gap into the cylinder volume as well as Carnot's shock loss and flow deflection in the valves. These factors contribute to a disturbance of the similarity concerning the resulting frequency. Instead of the expected increase by $\psi^{-2} = 1.98$ for operating points close to the optimum design point, the frequency is increased by a factor of 1.5 only. At the borders of the operating range, i. e. approaching either $\Pi = 1$ or the maximum pressure ratio Π_{max}, no increase of the frequency can be detected.

In a second step, the numerical model was used to further optimize the dimensions in terms of maximizing the exergy transferred to the compressed air flow $\Delta\dot{E} = N\Delta E$ for ambient pressure under variation of the lengths of the heater, the cooler, and the displacer, as well as the width of the annular gap. For this purpose, the simulation of complete operating curves and the determination of their maximum with respect to $\Delta\dot{E}$ were used as the input for an optimization algorithm. The resulting optimum operating curves are additionally shown in Fig. 3. The performance optimization compared to pure scaling is mainly achieved by an increased frequency due to lower flow pressure losses in a wider annular gap. The conveyed mass per cycle is almost unaffected, as the influence of the reduced mechanical losses exceeds the negative influence of the reduced heat transfer and the additional dead volume. To ensure a resilient comparability, these calculation results do not include leakage, so it is foreseeable that experimental results will show a reduced performance. Table 3 summarizes the geometric dimensions of the original single-stage prototype, the pure scaling, and the optimization result, which is the final design.

To minimize the experimental effort while maintaining the opportunity to perform all the investigations of interest, a three-stage cascade was realized, so that the middle stage is largely decoupled from external control. Fig. 4 shows the schematic flowchart of the test stand, which has been optimized beyond that of the single-stage prototype [24]. Please refer to the Appendix for a list of the sensors and data acquisition modules used at the various measurement points, including their IDs and specifications.

The cycle pressure in the stages is measured by piezoresistive absolute pressure sensors in the cold cylinder volumes. However, these signals are the only ones that are recorded with a high temporal resolution

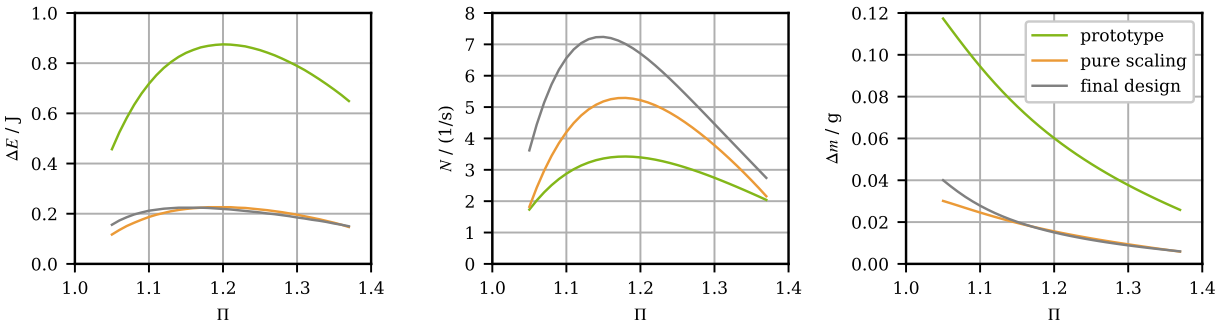

(a) Exergy gain of the compressed air per cycle (b) Frequency (c) Conveyed mass per cycle

Fig. 3. Calculated operating curves for single-stage prototype, pure scaling by $\psi = 0.71$ and the optimized and realized stage for ambient pressure, $T_h = 295$ °C and $T_c = 15$ °C neglecting leakage and additionally increased friction losses.

Table 3
Geometrical dimensions of the prototype, pure scaling by $\psi = 0.71$, and the realized stage.

Quantity	Symbol	Prototype [24]	Pure scaling ($\psi = 0.71$)	Realized stage
Max. stroke amplitude	$\hat{x}$	25 mm	12.5 mm	12.5 mm
Displacer diameter	d_D	82.5 mm	58.34 mm	67.1 mm
Displacer wall thickness	s_D	1.25 mm	0.88 mm	0.59 mm
Displacer length	l_D	256 mm	128 mm	145 mm
Annular gap width	s_{gap}	1.2 mm	0.85 mm	1.2 mm
Cylinder wall thickness	s_C	1.15 mm	0.71 mm	1.2 mm
Cooler length	l_c	88 mm	44 mm	50 mm
Heater length	l_h	85 mm	42.5 mm	51 mm
Displacer rod diameter 1	$d_{r,1}$	20 mm	14.55 mm	16 mm
Displacer rod diameter 2	$d_{r,2}$	14 mm	10.29 mm	12 mm
Length bushing 1	l_{b1}	35 mm	17.5 mm	25 mm
Length bushing 2	l_{b2}	25 mm	12.5 mm	20 mm
Spring constant	C_S	0.1 N/mm	0.1 N/mm	0.105 N/mm

to trace the thermodynamic cycle in each stage, and are therefore also used to determine the operating frequencies. The additional monitoring of the displacer positions by linear variable differential transformers (LVDTs) was dropped for reasons of simplicity and to avoid the risk of additional friction as observed during the experiments with the first prototype. Since the prediction of a nearly saw tooth-shaped motion has already been experimentally confirmed, the pressure signal is considered to provide sufficient information about the displacer motion. Furthermore, pressure sensors are installed in the additional buffer volumes upstream and downstream of the cascade, and also in the small buffers between the stages, so that the individual stage pressure ratios can be determined.

Since a three-stage cascade is not expected to reach industrially relevant pressure levels above 6 bar, the pressure in the upstream buffer volume can be controlled using the compressed air supply of the laboratory. To preset a total pressure ratio $\Pi_{tot} = p_3/p_0$ across the cascade, the outlet pressure p_3 downstream of the cascade is software-controlled via a solenoid control valve. Behind the valve, the mass flow of the

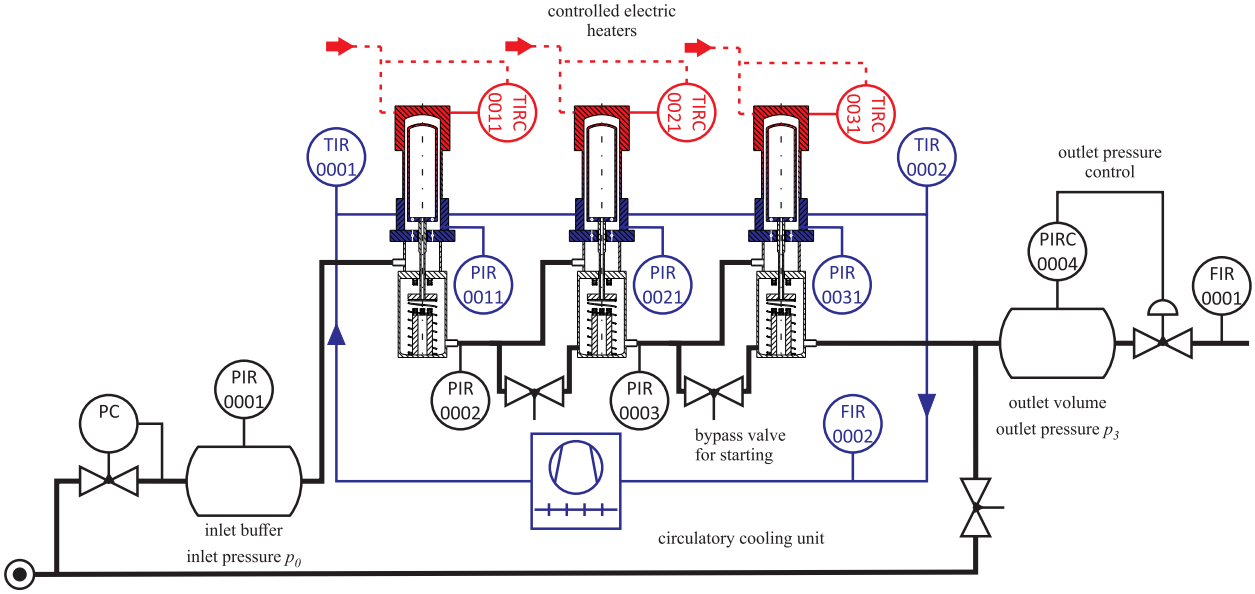

Fig. 4. Schematic flowchart of the test stand for the three-stage cascade.

conveyed air is detected by a high-precision flow meter at ambient pressure, before it is released to the atmosphere. These parts of the instrumentation have already proven their worth on the prototype test stand and have therefore been retained in the same way as the bypass to fill the downstream buffer volume. Similarly, additional bypasses were installed between the stages to preset the individual stage pressure ratios, so that the corresponding preliminary simulations [25] can be reproduced and validated.

To reduce the error of the pressure measurements to a minimum far below the specified sensor accuracy [30], all pressure signals were calibrated with a high-precision reference at the beginning of each measurement series. Exploiting both calibrated ranges of the high-precision flow meter, the measurement error of the mass flow is reduced to a technical minimum. Consequently, the error of the exergy gain is also reduced, since it is essentially a product of the mass flow and the logarithm of the pressure ratio. All measured quantities were averaged over five full cycles to further reduce errors caused by statistical scattering of the readings. The temperature sensors were calibrated in a thermostat bath using a high-precision reference resistance thermometer.

In a practical application, the stages are heated consecutively by a flue gas stream or an alternative medium with suitable thermal properties, so that the heater temperature decreases from the first to the last stage depending on its heat capacity rate. Since this effect is relatively easy to model within the LabVIEW program, no heat carrier fluid, such as a thermal oil, as originally envisaged by Fischer et al. [25], is used to heat the stages on the test stand. Instead, each heater is heated electrically, and their temperatures are individually controlled. Each heater is therefore equipped with eight circularly arranged heating cartridges of 125 W nominal power and four thermocouples. Three of these are radially distributed, and one is integrated in a cartridge. The former are used to evaluate the average temperature of a heater, and the latter as a cartridge temperature limiter and as input to the slave controller of a cascade control. This greatly reduces the experimental effort and, above all, the safety risks associated with thermal oils at temperatures above 200 °C. Moreover, this heating method offers the opportunity to take into account avoidable heat losses, which would not occur, if the machine design were optimized for series production, as further explicated in section 3.2. A CFD simulation was performed to ensure a nearly uniform temperature distribution inside the stainless steel heater in steady-state operation, which was subsequently confirmed by the experiments, as the temperature differences between the measurement points were less than 4 K. The heaters are insulated with high-temperature ceramic fiber sheets of 25 mm thickness. As illustrated in Fig. 2, one layer was used at the top, two around the heater, and three around the cylinder wall in the regenerator section. Fig. 5 shows the experimental thermocompressor cascade installed on the test stand.

3.2. Avoidable heat losses

As already detected by initial analytical modeling [9], one of the challenges of thermocompressors is their relatively low power density. Although a cascade consisting of a sufficient number of consecutive stages can reach the pressure level of a typical compressed air application, the mass flow demand will in most cases additionally require an arrangement of several cascades in parallel. Such a concept results in a two-dimensional array of closely adjacent consecutive and parallel machines, so that both heating and cooling can be realized by common flow channels. In contrast to the experimental machine, convection and radiation from the heaters to the ambience are less relevant in this case. In addition, series production techniques such as deep drawing, which were not available for the experimental machines, would easily allow the wall thickness of the cylinder to be reduced from $s_C = 1.2$ mm to e.g. $s_C = 0.5$ mm, i.e. by a factor $f_C = 0.5/1.2 \approx 0.42$, without exceeding the material strength and to even lower values in case of the displacer, thus significantly reducing the thermal conduction losses.

To evaluate the convective, radiative, and conductive losses of the experimental setup, the heating power P_h of all stages was recorded at standstill for different heater temperatures and a constant cooler temperature of 15 °C. Fig. 6 shows the results compared to an analytical estimate. The heat flow summarized as “convection and radiation” and displayed in light gray is iteratively calculated, assuming free convection at the cylinder wall and top [31]. Compared to the heater, the ambience is large and is therefore treated as a black radiator. In

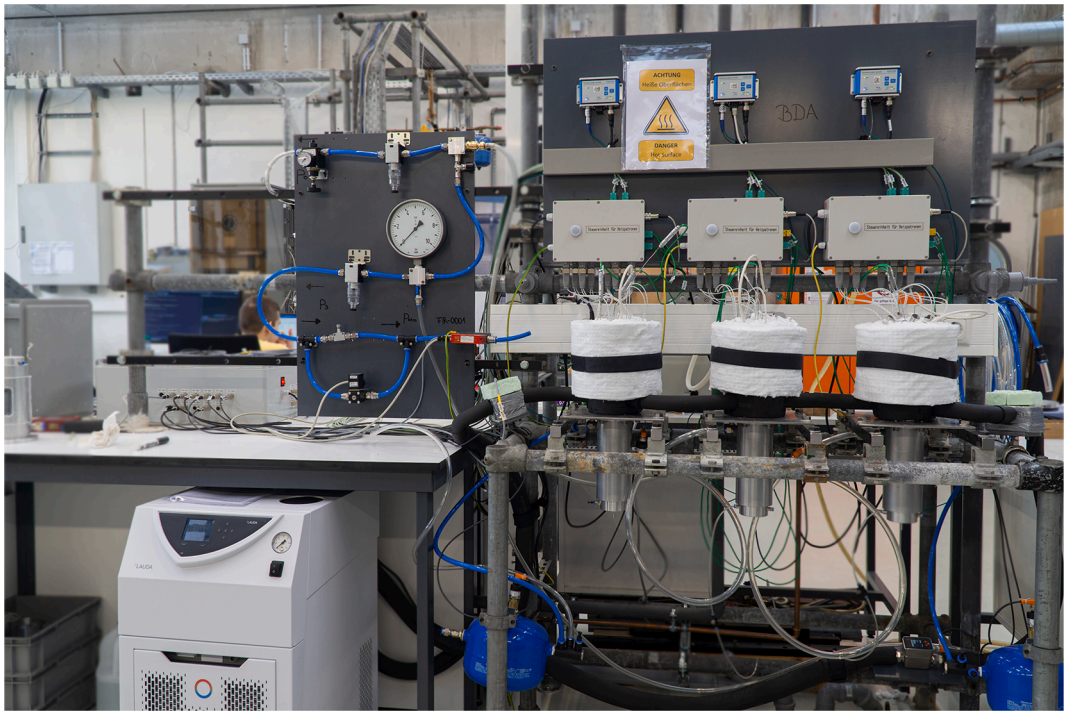

Fig. 5. Photo of the thermocompressor cascade and the test stand.

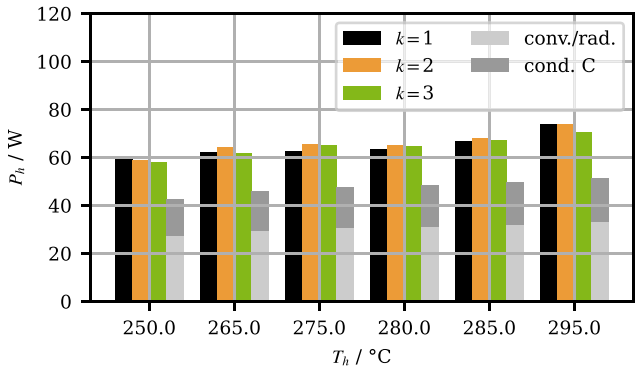

Fig. 6. Heater power at standstill for different heater temperatures T_h and constant cooler temperature $T_c = 15$ °C.

addition, the heat flow due to axial conduction along the cylinder wall is shown in darker gray. Since the stages are identical, the measured heating power is almost the same at each temperature. Minor deviations may be attributed to a slightly scattering quality of the insulation.

The analytically predicted losses underestimate the heating power for all temperatures. This is mainly due to the additional losses via the displacers and the laboratory ventilation, which causes an air circulation that exceeds the air flows typically induced by free convection, but cannot be accounted for analytically.

A linear function $\dot{Q}_{av}(T_{h,k})$ was fitted to the calculation results for the convective and radiative losses at various heater temperatures $T_{h,k}$ and implemented in the LabVIEW program. Based on this function, and assuming a reduction of the cylinder wall thickness by the aforementioned factor $f_C = 0.42$, the actual heater power $P_{h,k}$ of stage k is correspondingly reduced, when its effective heater temperature $T_{h,k}$ is calculated on the basis of the preset virtual heat capacity rate $\dot{W}_h$ and the outlet temperature $T_{h,k-1}$:

$$T_{h,k} = T_{h,k-1} - \frac{P_{h,k} - (1 - f_C)\dot{Q}_{cond}(T_{h,k}) - \dot{Q}_{av}(T_{h,k})}{\dot{W}_h} \tag{12}$$

The preset temperature T_h corresponds to the inlet temperature $T_{h,0}$ of the virtual heat carrier fluid at the first stage. The outlet temperature $T_{h,1}$, which is the actual heater temperature, equals the inlet temperature of the second stage, and so on. Thus, all outlet temperatures can be evaluated successively.

4. Experimental results

4.1. Steady-state operation of the single stages

Four technically identical stages were manufactured, but the initial setup of the first prototype [24] showed that even small variations within the accepted manufacturing tolerances had a large impact on the performance of the machine. Therefore, all stages were tested separately in single-stage operation to compare their performance with each other and with the simulation results.

Fig. 7 shows the experimental operating curves of the three stages, which were further investigated, for a variation of the preset pressure ratios at ambient inlet pressure. Evidently, stages 2 and 3 exhibit very similar operating characteristics in terms of the exergy transferred to the compressed air flow, frequency, and conveyed mass flow. Their general shape matches the results from the first prototype. Merely at low pressure ratios, stage 3 performs better due to a slightly higher frequency. Obviously, stage 1 exhibits higher leakage rates due to poorer manufacturing accuracy of the displacer rod or bushing. As a result, the maximum experimentally achievable pressure ratio, as well as the conveyed mass flow and, correspondingly, the exergy transferred to the compressed air flow, are significantly lower. Unfortunately, this deficiency was not remediable, so the stage had to be used for the cascade. Although the first stage limits the overall performance of the cascade, the order of the stages should be chosen in such a way that the resulting overall impact of the leakage is minimized. Since laminar flow may be assumed in the bushing gaps according to the results presented in [24], the leakage mass flows increase with the square of the corresponding stage inlet pressure, since both the density and the volume flows are linearly dependent on it. Primarily, the latter are linear functions of the absolute pressure differences between the buffers and between the active cycle volume and the inlet buffer, which act across the lower and the upper bushing, respectively, and these are in turn proportional to the stage inlet pressure for a given pressure ratio. So, the stages were arranged in order of decreasing leakage rates to minimize their overall impact on the performance of the cascade.

In general, stages 2 and 3 agree well with the modeled results, which are also shown in Fig. 7. To generate these results, the expected leakage flows had to be included in the model. However, it is noteworthy that for these stages, the correction factors $f_{leak,1}$ and $f_{leak,2}$ for the upper and the lower bushing, which account for unpredictable additional effects such as eccentricity and misalignment, could be reduced to 6 and 8, respectively, whereas values of 20 were required to reproduce the experimental results of the single-stage prototype [24]. This indicates that the leakage was reduced even though water was not used to seal the bushings anymore. However, the effect of speed-independent dry friction had to be added to the model to match the experimental results, indicating an additional effect of the dry-running bronze bushings.

Due to the reduction of the leakage rates compared to the single-stage prototype, the practical upper limit of the pressure ratio Π_{lim} is closer to the theoretical maximum pressure ratio, which is $\Pi_{max} = 1.45$ according to the second-order model neglecting leakage. For stages 2 and 3, the ratio of the practical and the theoretical maximum pressure gain, which equals the fraction $(\Pi_{lim} - 1)/(\Pi_{max} - 1)$, reaches values of 79 % and 81 %, respectively. This is a significant improvement,

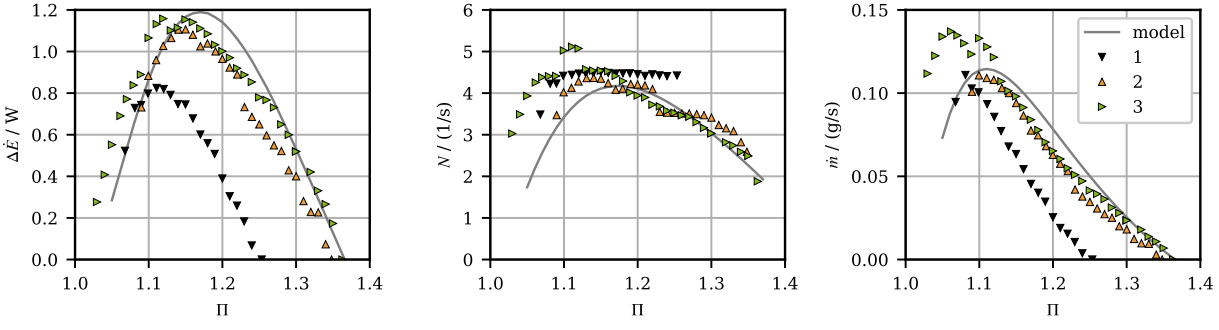

(a) Exergy gain of the compressed air flow (b) Frequency (c) Mass flow

Fig. 7. Experimental operating curves #1, #2, and #3 according to Appendix for the stages in single-stage operation in comparison to the model results at ambient inlet pressure, $T_h = 295$ °C and $T_c = 15$ °C [32].

compared to 67 % for the first single-stage prototype [24]. As already apparent in Fig. 7, only stage 1 exhibits a poorer performance, corresponding to a value of 56 %. Furthermore, stages 2 and 3 reach a power density of approximately 12.5 W per liter of displacement at the pressure ratio Π_{exm}, where the exergy gain of the compressed air flow according to Fig. 7 (a) is maximum. This is a major enhancement compared to the first prototype, which only reached 7.1 W/l. Table 4 summarizes all characteristic maximum and limiting values derived from the experimental data in Fig. 7, including the analytically predicted lower stability limit, i.e. the lowest pressure ratio $\Pi_{0,K2}$, at which steady-state operation of the stage is theoretically possible [25].

4.2. Steady-state operation of the cascade

4.2.1. Operation at a preset heater temperature

Similarly to the single-stage experiments, the multi-stage experiments were conducted by operating the cascade with a closed outlet buffer to determine the practical upper limit of the total pressure ratio $\Pi_{tot,lim}$, and then gradually reducing the total pressure ratio. During the experiments, values slightly above 2.1 could be achieved for $\Pi_{tot,lim}$, but no reliable data could be measured, as stage 3 no longer operated steadily under these conditions. This pressure ratio is lower than the product of the practical upper limits in single-stage operation of the three stages according to Table 4, because the leakage flows are increased due to the larger pressure differences across the higher stages. This effect was already recognized during experiments with the first prototype at higher inlet pressures [24].

Fig. 8 (a) shows the exergy gain of the compressed air flow $\Delta\dot{E}$ for the entire cascade as well as for each stage for various total pressure ratios Π_{tot}. Stable operation of all active stages was achieved over the entire range of pressure ratios shown, which essentially confirms the self-regulation ability of the multi-stage thermocompressor with overdriven free displacers. So far, this had only been predicted by analytical models and simulations [25]. Furthermore, the qualitative course of the exergy gain agrees with the multi-stage simulations in MATLAB/Simulink, although the latter were carried out with a different machine design, so that a quantitative comparison is not possible. It shows a maximum of approximately 3 W at $\Pi_{tot} = 1.46$. The resulting stage pressure ratios Π_k are listed in Table 5. They are nearly the same as those of the single stages at their optimum operating points according to Table 4. Hence, the pressure ratio of the cascade at its optimum operating point $\Pi_{tot,exm}$ is only slightly lower than the product of the pressure ratios at the optimum operating points of the single stages. The courses of the exergy gain of each stage agree well with the simulation results, as it is lowest for the first stage and increases with the inlet pressure p_{k-1}. This difference decreases with increasing Π_{tot}, as all stages reach their practical upper limit.

The experiments also confirm the existence of lower stability limits $\Pi_{k,lsl}$ for the operation of each stage. The first stage stops, when the total pressure ratio is decreased below 1.36, as indicated by the vertical dashed line. At this point, the stage pressure ratio Π_1 drops below 1.08, which corresponds to the analytically estimated stability limit $\Pi_{0,K2}$ according to Table 4. A further reduction of Π_{tot} below 1.17 results in Π_2 undercutting 1.09, and consequently, the second stage stops. This pressure ratio is indicated by the vertical dash-dotted line and is again in good agreement with the analytical prediction. When only the third stage is operating, the total exergy gain of the compressed air flow is less than that of the single stage because the flow pressure losses in the stopped stages must be compensated.

As soon as a stage stops, the product of the pressure ratios of the remaining stages must equal Π_{tot}, so that these undergo a sudden leap. The course of the stage pressure ratios Π_k shown in Fig. 8 (c) qualitatively agrees with the simulation results presented by Fischer et al. [25], as all stage pressure ratios Π_k increase with increasing Π_{tot}. In addition, Π_k increases in the flow direction from stage to stage for the operating points between the lower stability limit $\Pi_{0,K2}$ and approximately Π_{exm}. In the range above, only the pressure ratios of the last two stages converge, whereas the first stage lags behind due to its higher leakage rate.

Unfortunately, the leakages discussed in section 4.1 also affect the course of the frequencies in Fig. 8 (d) significantly. The expected decrease at total pressure ratios above $\Pi_{tot,exm}$ is only marginally observed for stages 2 and 3. Due to the higher leakage rates, the frequency of stage 1 even increases, because it would otherwise not convey the required mass flow. The difference between stage 2 and stage 3 may be attributed to the effect of the different leakage rates again, which becomes more dominant at higher pressure levels.

At total pressure ratios around $\Pi_{tot,exm}$ and somewhat above, all stages run at almost the same frequency, except for one outlier. This was only expected for a single operating point, but within this range, the stages evidently synchronize due to the relatively small buffers and oscillations of the common mounting rack.

Nevertheless, the above experimental results prove that a stable operation of cascaded thermocompressors with overdriven free displacers is feasible in a wide range of pressure ratios, even though stage 1 of this experimental setup performs significantly poorer due to tolerance issues, which will, however, be less severe in a future series production than in the current individual manufacture, and therefore be acceptable.

4.2.2. Operation for a virtual heat capacity rate of a heating fluid

In a practical application, the heat input to a thermocompressor cascade would be provided by a fluid enthalpy flow such as a flue gas stream flowing along the heaters, so that its temperature is successively reduced [9]. As motivated in section 3.1, this effect was emulated in the experiments by controlling the heater temperature of each stage according to section 3.2, particularly Eq. (12). In this operation mode, the preset temperature corresponds to the inlet temperature $T_{h,0}$ of the fluid at the first stage. All heater temperatures are automatically adjusted depending on the heat flow absorbed by each stage and the preset virtual heat capacity rate $\dot{W}_h$. Disregarding any constant prefactors, the ideally absorbed heat flow of each stage k according to the isothermal analysis [9] features the following dependences:

$$\dot{Q}_{h,ideal,k} \sim p_{k-1}^2 \widehat{V} \frac{(\Pi_{max} - \Pi_k)^2}{\Pi_{max} - 1} (\ln\Pi_k)^2 \tag{13}$$

It is a function of the inlet pressure p_{k-1}, the volume amplitude $\widehat{V}$, the stage pressure ratio Π_k and the maximum pressure ratio Π_{max}. The latter depends on the geometry of the machine and particularly on the temperature ratio, or rather the on heater temperature in case of a nearly constant cooler temperature. Compared to the experiments presented in section 4.2, an even more complex, highly non-linear equation system thus arises, since the heater temperatures constitute additional degrees of freedom. The stability analysis based on the isothermal model was therefore carried out for constant heater temperatures, but simulations of a multi-stage cascade indicated that stable operation is also achieved in this case [25].

Fig. 9 shows an operating curve consisting of multiple stable operating points at different pressure ratios, thus confirming the prediction. Since $T_{h,0} = 295\,^{\circ}\mathrm{C}$ was set as the inlet temperature of the virtual enthalpy flow, all heaters have a lower temperature compared to the

Table 4
Summary of the single-stage operating characteristics extracted from the operating curves #1, #2, and #3 in Fig. 7.

k	1 (#1)	2 (#2)	3 (#3)
Π_{exm}	1.11	1.15	1.15
N_{exm} / s^{-1}	4.43	4.35	4.54
$\dot{m}_{exm}$ / (g/s)	0.093	0.094	0.098
Π_{lim}	1.25	1.35	1.36
$(\Pi_{lim} - 1)/(\Pi_{max} - 1)$	0.56	0.79	0.81
$\Pi_{0,K2}$	1.08	1.10	1.11

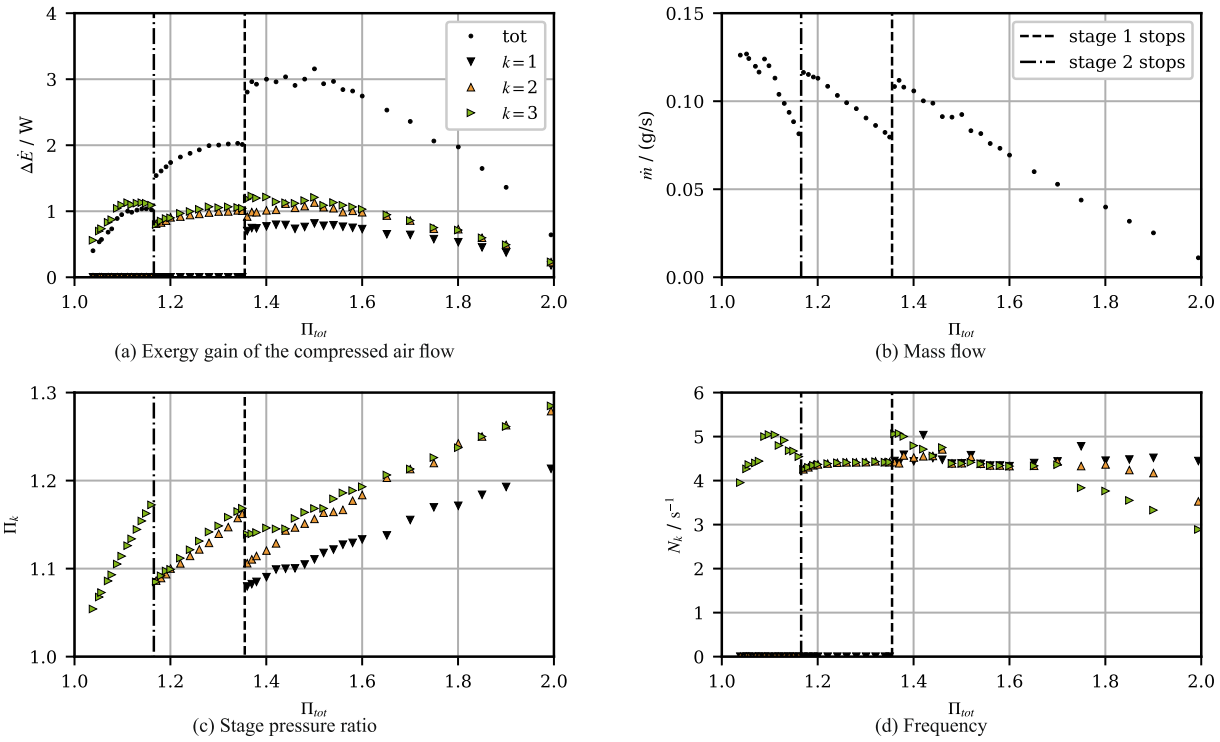

Fig. 8. Experimental operating curves for ambient pressure, $T_h = 295$ °C and $T_c = 15$ °C (#4) [32].

Table 5
Significant operating data of the stages extracted from the operating curve #4 according to Appendix.

k	1	2	3
$\Pi_{k,exm}$	1.104	1.15	1.16
$N_{k,exm}/s^{-1}$	4.39	4.39	4.39
$\Pi_{k,lsl}$	1.08	1.09	1.05

operation at constant heater temperature. The total exergy gain of the cascade and the maximum achievable pressure ratio are reduced accordingly.

The absorbed heat flow shown in Fig. 9 (e) represents the power of the electric heater reduced by the avoidable heat losses introduced in section 3.2 and therefore corresponds to the temperature differences $\Delta T_{h,k} = T_{k-1} - T_k$ across each stage k. Only for stage 3, the course of the absorbed heat flow meets the expectations, as it is similar to the exergy gain of the compressed air. The proportionality factor is of course significantly lower than according to the isothermal theory, since the latter is based on the idealized assumption that the exergy of the absorbed heat is entirely transferred to the compressed air, except for the share that is converted to p,V-work by the piston rod plunging into the cold cylinder volume. Because of the various loss mechanisms, this is not the case for a real machine. The course of the absorbed heat flows of stages 1 and 2 is influenced by increased leakage flows, which cause these stages to operate at pressure ratios Π_k significantly below the maximum pressure ratio, even though the total pressure ratio Π_{tot} is increased. Therefore, a sufficient mass flow is only conveyed if the frequency of these stages increases.

Another effect of the leakage can be observed in the plot of the heater temperatures shown in Fig. 9 (f). The temperature of stage 3, which corresponds to the outlet temperature of the virtual fluid flow, is almost constant, whereas it should theoretically increase due to a reduced absorbed heat flow, when approaching the practical upper limit of the total pressure ratio. Because of their increased operating frequencies, stages 1 and 2 absorb even more heat. So, they operate at lower temperatures and thus compensate the expected (and actually observed) reduced heat absorption of stage 3. Only when stage 1 is not operating, the course of the heater temperature of stage 3 shows the expected increase after exceeding the pressure ratios of the respective optimum operating points. However, this additional degree of freedom does not impair the self-regulation capabilities of the system in any way.

Fig. 10 visualizes the influence of the heat capacity rate of the virtual heating fluid flow on the exergy transferred to the compressed air flow and the conveyed mass flow. For the displayed heat capacity rates and total pressure ratios between 1.4 and 1.8, all stages are operating. When decreasing the heat capacity rate, the temperature change of the virtual heater flow across each stage is increased, so that all stages operate at lower heater temperatures. Thus, the performance is reduced in the entire operating range. Since the temperature ratio affects the theoretically possible maximum pressure ratio, the practically achieved pressure ratio is reduced. This shifts the stability limits to slightly lower values and thus extends the stable operation range without stopping of any stage. This is of course undesirable, since an automatic restart of a single stopped stage without external intervention can unfortunately not be guaranteed.

A change in the compressed air demand has a similar stabilizing effect: Since the variation of the total pressure ratio can be interpreted as an imbalance between supply and demand, an increase in the latter will reduce the total pressure ratio. Assuming that the cascade has been running close to its practical upper limit, the absorbed heat flow will increase, as the stage pressure ratio is shifted toward the optimum operating point, and consequently, the heater temperatures will decrease. Therefore, the maximum achievable pressure ratio is reduced, and accordingly, the lower stability limit is shifted to lower values. This improves the overall performance, as all stages will continue to operate.

The exemplary variation of the heat capacity rate further proves the industrial applicability, as fully self-controlled steady-state operation is achieved even when the supplied heat capacity rate varies. This is an expected scenario when utilizing waste heat from industrial processes.

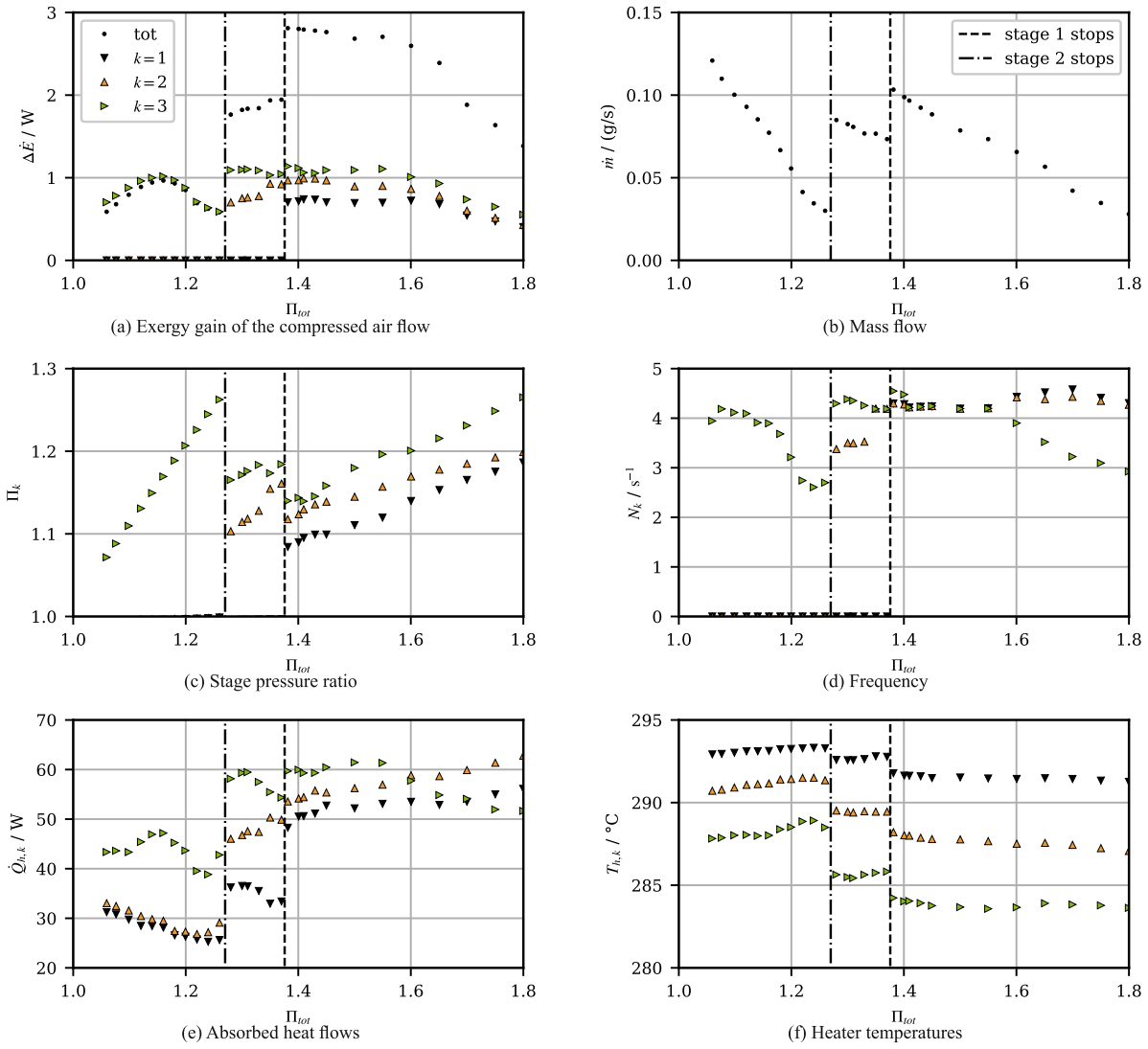

Fig. 9. Experimental operating curves for the cascade for ambient pressure, $T_{h,0} = 295$ °C and $T_c = 15$ °C (#5) for a heat capacity rate of 15 W/K [32].

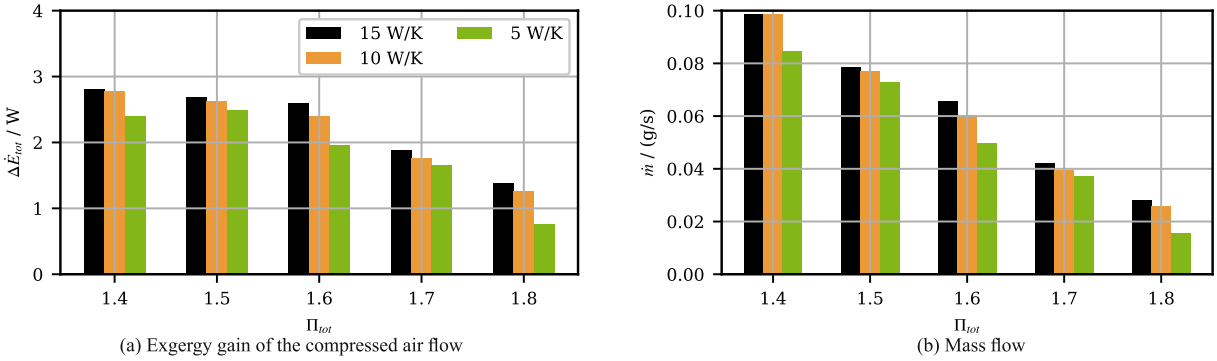

Fig. 10. Effect of three different virtual heat capacity rates $\dot{W}_h$. Data according to Appendix, curves #5, #6, and #7 [32].

4.3. Unsteady operation of the cascade

Even though the steady-state experiments show that the stages do not stop operation at the practical upper limit of the total pressure ratio, the restart capabilities of the cascade are of interest, particularly in comparison to previous simulation results based on a model implemented in MATLAB/Simulink, which explicitly reproduces the motion characteristics of the displacer [25]. As known from previous single-stage experiments [24], a restart is only possible if an initial pressure difference is preset. In the case of a cascade, this requires a pressure difference across each stage, which was realized by filling the outlet buffer up to 2 bar during standstill of the machine, while the bypasses between the stages were slightly opened. After closing the bypasses, p_3 is lowered by opening a valve to the ambiance, thus simulating a consumption of

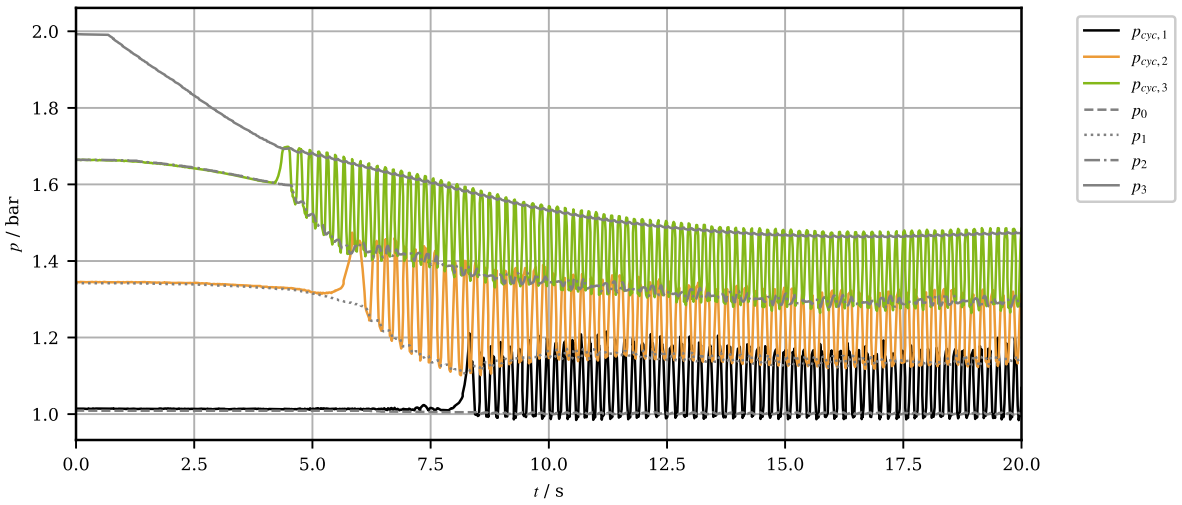

Fig. 11. Restart of all stages due to a pressure decrease in the outlet buffer (ambient pressure, $T_h = 295\,°C$, $T_c = 15\,°C$ [32]).

compressed air. Due to the unstable displacer, stage 3 starts to operate without any further external intervention, as illustrated in Fig. 11. As a result, p_2 is reduced as stage 3 absorbs air from the buffer between the stages.

Subsequently, stage 2 and stage 1 start as well. This successive starting of the stages confirms the results of previous simulations [25], which were performed for a thermocompressor featuring an overdriven free displacer, but a radially shifted design with separate shell-and-tube heat exchangers and a metal fiber regenerator. Therefore, the measurements cannot be directly compared with the simulation results.

5. Conclusion and outlook

Within this contribution, the feasibility of a three-stage thermocompressor cascade with overdriven free displacers was demonstrated experimentally for the first time. The expected self-excited and self-controlled operation without any external mechanical power supply was confirmed. Stable operation was achieved for a wide range of the total pressure ratio despite the complexity of the system with many mutually interacting parameters, particularly pressures, temperatures, and frequencies. Furthermore, it was demonstrated that this advantageous characteristic is not only achieved for a constant heater temperature, but also for dynamically fluctuating heater temperatures as expected when extracting waste heat from a fluid enthalpy flow. So, the experiments generally confirm the predictions by analytical and numerical models and the expectations based on the results of previous experiments with a first single-stage prototype.

Compared to this first prototype, the performance and the operational flexibility of the stages was significantly improved by replacing the water-lubricated polymer bushings by dry-running bushings made of bearing bronze, thereby reducing the leakage from the active cycle volume and the outlet buffer to the inlet buffer significantly. Unfortunately, the required tolerances could not be realized due to the individual manufacture of the components, so the stages did not perform equally. Instead, stage 1 features a lower practical limit of the pressure ratio and conveys a lower mass flow at a given pressure ratio than stage 2 and 3. Therefore, a future series production should focus on a reproducible fit of the displacer rod and the bushing. Nevertheless, these differences did not affect the general feasibility of the concept. Most of the predictions regarding the operating characteristics, such as the courses of the stage pressure ratio, the exergy transferred to the compressed air flow, or the mass flow, could be experimentally confirmed.

The similarity-based scaling procedure, which was used to scale the first single-stage prototype, proved to be a valid tool to determine the general dimensions of a new machine based on an existing design and provided new insights regarding the general dimensioning of the proposed thermocompressor cascades. The increase of the power density – in terms of exergy transferred to the compressed air flow – by scaling towards smaller geometrical dimensions was confirmed experimentally. The achieved value of 12.5 W per liter of displacement is almost double the power density of the single-stage prototype. However, a further downsizing will increase the manufacturing effort of the overall system due to the larger number of units required, and furthermore, the relative losses due to axial conduction in the cylinder will also increase. So, the present size is presumably a good compromise, but in the end, the optimum design will also depend on economic aspects and require a detailed profitability analysis of a sophisticated series design, depending on boundary conditions such as the compressed air demand and pressure level of the specific application.

Future developments should focus on transferring the existing design to a series machine, preserving the basic component geometries and functions, but optimizing their design for mass production techniques such as casting, extrusion, or deep-drawing. Additionally, a further reduction of the leakage by more accurate machining technologies for the combination of displacer rod and bushing should be pursued.

Although there is still potential for improvements in the details of the constructional design regarding the development of a series machine, a guideline for the design of a thermocompressor cascade with overdriven can be derived on the basis of the presented findings. As a first step, the single stages should be optimized for maximum power density based on the available temperature level of the waste heat. This allows a low-cost mass production of identical stages. The required total pressure ratio then determines the number of stages for a specific application. To match the compressed air demand or the available waste heat, multiple cascades may be arranged in parallel. Thus, a two-dimensional array of adjacent stages is formed, which can easily be supplied with common flows for both heating and cooling, as the stages can be designed in a way, that flow channels are formed automatically, when the stages are placed side by side. The resulting typical stage pressure ratio should be between the optimum operating point and the practical upper limit in order to make optimum use of the self-controlling abilities and to ensure the continuous operation of all stages.

6. Data availability

Datasets related to this article can be found at https://zenodo.org/doi/https://doi.org/10.5281/zenodo.10726184, an open-source online data repository hosted at ZENODO [32].

Declaration of competing interest

The authors declare that they have no known competing financial interests or personal relationships that could have appeared to influence the work reported in this paper.

Acknowledgments

This research was funded by the German Research Foundation (DFG), grant number KU 755/5-2.

Appendix

Table A1
Instrumentation of the test stand.

Measurement point ID	Type of sensor	Model name	Measuring range	Maximum error
FIR–0001	Thermal mass flow meter	Vögtlin GSM-C4TA-BN00	0,2 … 20 ln/min 0,04 … 4 ln/min	±0.3 % of full scale +±0.5 % of reading
FIR–0002	Magnetic-inductive flow meter	IFM SMK12XGXFRKG/US-100	0.05 … 35 l/min	0,2 % of full scale + ± 0,8 % reading
PIR–00X1	Pressure transmitter	Kistler 4011A010DSL81-2,0	0 … 10 bar	±0.3 % of full scale
PIR–000X	Pressure transmitter	IFM PT-010-AFG14-A-ZVG/US	0 … 10 bar	±0.5 % of full scale (BFSL)
TIR–000X	Resistance thermometerPT100 Class A	Sontec 800-029TT6-045-A-A-4l-S-2,0-ADE	−40 … 180 °C	±0.15 K + 0.2 % of reading
TIR–00X1, TIR–00X2, TIR–00X3	Thermocouple Type KClass 1	B+B K-H625 0150–15	−200 … 1100 °C	±1.5 K

Table A2
Data acquisition modules used.

Module name	Description	Quantity	Measuring points / Outputs /Modules
NI cDAQ-9178	8-slot USB Chassis for C Series Modules	1	NI-9253, 3x NI-9210, NI-9217, NI-9269
NI-9253	50 kS/s/Channel, ±20 mA, 24-Bit, 8-Channel C Series Current Input Module	1	FIR 0001, GIR 0001, PIR 0011, PIR 0001, PIR 0002
NI-9210	4-Channel, 14 S/s Aggregate, ±80 mV C Series Temperature Input Module for Thermocouples	3	TIR 0011, TIR 0012, TIR 0013, TIR 0014, TIR 0021, TIR 0022, TIR 0023, TIR 0024, TIR 0031, TIR 0032, TIR0033, TIR 0034
NI-9217	4-Channel, 400 S/s Aggregate, 0 Ω to 400 Ω, PT100 RTD C Series Temperature Input Module	1	TIR 0001, TIR 0004
NI-9269	100 kS/s/Channel Simultaneous, ±10 V, Isolated, 4-Channel C Series Voltage Output Module	1	Heater controls 1, 2, 3
NI USB-6211	16 Analog Input (16-Bit, 250 kS/s), 2 Analog Output (250 kS/s), 4 Digital Input, 4 Digital Output USB Multifunction Input/Output Device	1	Control valve

Table A3
Overview of measured operating curves [32].

#	Source Name	Heater Control	In Figures	Comment
1	KAS_exp_100_295_15_stat_BK_108	Load-independent constant heater temperature	Fig. 7	Single-stage operation of stage 1
2	KAS_exp_100_295_15_stat_BK_210	Load-independent constant heater temperature	Fig. 7	Single-stage operation of stage 2
3	KAS_exp_100_295_15_stat_BK_405	Load-independent constant heater temperature	Fig. 7	Single-stage operation of stage 3
4	KAS_exp_100_295_15_stat_BK_014	Load-independent constant heater temperature	Fig. 8	
5	KAS_exp_100_295_15_stat_BK_040	Virtual heat capacity $\dot{W}_h = 15$ W/K	Fig. 9, Fig. 10	
6	KAS_exp_100_295_15_stat_BK_030	Virtual heat capacity $\dot{W}_h = 10$ W/K	Fig. 10	
7	KAS_exp_100_295_15_stat_BK_032	Virtual heat capacity $\dot{W}_h = 5$ W/K	Fig. 10	

References

[1] Unger, M. and Radgen, P. (2018) Energy Efficiency in Compressed Air Systems: A review of energy efficiency potentials, technological development, energy policy actions and future importance, in *Proceedings of the 10th International Conference on Energy Efficiency in Motor Driven Systems (EEMODS' 2017)* (ed P. Bertoldi), 6.-8.09.2017, Rome, Italy. Publications Office of the European Union, Luxembourg, pp. 207–233.

[2] Sauer, A. and Schneider, C. (2021) *Energieeffizienz in der Industrie: Empirische Analysen, Auswertungen und Handlungsempfehlungen*, Hanser, München. 978-3-446-46650-0.

[3] S. Brückner, L. Miró, L.F. Cabeza, M. Pehnt, E. Laevemann, Methods to estimate the industrial waste heat potential of regions – A categorization and literature review, Renew. Sustain. Energy Rev. 38 (2014) 164–171, https://doi.org/10.1016/j.rser.2014.04.078.

[4] L. Miró, S. Brückner, L.F. Cabeza, Mapping and discussing Industrial Waste Heat (IWH) potentials for different countries, Renew. Sustain. Energy Rev. 51 (2015) 847–855, https://doi.org/10.1016/j.rser.2015.06.035.

[5] M. Papapetrou, G. Kosmadakis, A. Cipollina, U. La Commare, G. Micale, Industrial waste heat: Estimation of the technically available resource in the EU per industrial sector, temperature level and country, Appl. Therm. Eng. 138 (2018) 207–216, https://doi.org/10.1016/j.applthermaleng.2018.04.043.

[6] C. Forman, I.K. Muritala, R. Pardemann, B. Meyer, Estimating the global waste heat potential, Renew. Sustain. Energy Rev. 57 (2016) 1568–1579, https://doi.org/10.1016/j.rser.2015.12.192.

[7] Bundesamt für Wirtschaft und Ausfuhrkontrolle (2023) *Gesetz zur Steigerung der Energieeffizienz in Deutschland 1 (Energieeffizienzgesetz - EnEfG)*.

[8] S. Thomas, E.J. Barth, Active Stirling Thermocompressor: Modelling and effects of controlled displacer motion profile on work output, Appl. Energy 327 (2022) 120084, https://doi.org/10.1016/j.apenergy.2022.120084.

[9] F. Fischer, H.-D. Kühl, Analytical model for an overdriven free-displacer thermocompressor, Appl. Therm. Eng. 185 (2021) 116251, https://doi.org/10.1016/j.applthermaleng.2020.116251.
[10] Blagin, E., Uskov, I., Kuznetsova, E., Dovgyallo, A. (2020) Development of Thermocompressor Mathematical Model Considering Hydraulic Losses in Regenerator, in *2020 International Multi-Conference on Industrial Engineering and Modern Technologies (FarEastCon)* (ed Institute of Electrical and Electronics Engineers), 06.-09.10.2020, Vladivostok, Russia. IEEE, pp. 1–7. doi: 10.1109/FarEastCon50210.2020.9271643.
[11] A.P.M. Glassford, Adiabatic cycle analysis for the valved thermal compressor, J. Energy 3 (5) (1979) 306–314, https://doi.org/10.2514/3.48007.
[12] Arquès, P. (1997) Piston movement in thermocompressor, in *Proc. 32nd IECEC* (ed American Institute of Chemical Engineers), 27.07.-01.08.1997, Honolulu, HI, USA, 1003-1008. doi: 10.1109/IECEC.1997.661906.
[13] Kornhauser, A.A. (1996) Analysis of an idealized Stirling thermocompressor, in *Proc. 31st IECEC* (ed Institute of Electrical and Electronics Engineers), 11.-16.08.1996, Washington, DC, USA, pp. 1331–1336. doi: 10.1109/IECEC.1996.553909.
[14] Arquès, P. (1998) Thermodynamical cycle analysis of gas in a Thermocompressor, in *Proc. 33rd IECEC* (ed American Nuclear Society), 02.-.06.08.1998, Colorado Springs, CO, USA.
[15] H. Karabulut, Thermodynamic analysis of bush engine, Gazi Univ. J. Sci. 16 (1) (2003) 135–144.
[16] W.-Y. Lin, X.-H. Wu, J.-L. Yang, L.-W. Yang, Experimental study and numerical analysis of thermocompressors with annular regenerators, Int. J. Refrig. 36 (4) (2013) 1376–1387, https://doi.org/10.1016/j.ijrefrig.2013.02.006.
[17] E. Blagin, A. Dovgyallo, D. Uglanov, H.F. Abdul Amir, P.S. Khiew, Study of different factors influence on thermocompressor performance, MATEC Web Conf. 108 (2017), https://doi.org/10.1051/matecconf/201710804001.
[18] R. Ibsaine, J.-M. Joffroy, P. Stouffs, Modelling of a new thermal compressor for supercritical CO_2 heat pump, Energy 117 (2016) 530–539, https://doi.org/10.1016/j.energy.2016.07.017.
[19] Hofacker, M.E., Kumar, N.S., Barth, E.J. (2014) Dynamic Simulation and Experimental Validation of a Single Stage Thermocompressor for a Pneumatic Ankle-Foot Orthosis, in *Proceedings of the ASME/BATH Symposium on Fluid Power and Motion Control 2013 (FPMC2013): Presented at ASME/BATH 2013 Symposium on Fluid Power and Motion Control, October 6-9, 2013, Sarasota, Florida, USA*, 6.10.2013-9.10.2013, Sarasota, FL, USA. ASME, New York. doi: 10.1115/FPMC2013-4483.
[20] A. Winkelmann, E.J. Barth, Design, modeling, and experimental validation of a stirling pressurizer with a controlled displacer piston, IEEE/ASME Trans. Mechatron. 21 (3) (2016) 1754–1764, https://doi.org/10.1109/TMECH.2015.2499706.
[21] Thomas, S. (2022) An Active Stirling Thermocompressor: Dynamic Modeling and Control. Vanderbilt University Dissertation.
[22] Edwards, M.J. (2005) Design, Modeling, and Performance of Miniature Reciprocating Thermocompressor. Oregon State University Master Thesis.
[23] Thomas, S. and Barth, E.J. (2017) Multi-Stage Modeling of a Stirling Thermocompressor, in *Proceedings of the ASME/BATH 2017 Symposium on Fluid Power and Motion Control (FPMC2017)*, 16.10.2017, Sarasota, FL, USA. doi: 10.1115/FPMC2017-4320.
[24] F. Fischer, H.-D. Kühl, Generation of compressed air by overdriven free-displacer thermocompressors – Experimental investigation of a single stage, Appl. Therm. Eng. 244 (2024) 122712, https://doi.org/10.1016/j.applthermaleng.2024.122712.
[25] F. Fischer, S. Peveling, H.-D. Kühl, Simulation and stability analysis of a thermocompressor cascade with overdriven free displacers, Therm. Sci. Eng. Prog. 44 (2023) 102037, https://doi.org/10.1016/j.tsep.2023.102037.
[26] Fischer, F. and Kühl, H.-D. (2023) Experimental data for a single-stage overdriven free-displacer thermocompressor (1.0) [Data Set]. doi: 10.5281/ZENODO.8289373.
[27] Urieli, I. and Berchowitz, D.M. (1984) *Stirling Cycle Engine Analysis*, Adam Hilger Ltd, Bristol. 0-085274-435-2.
[28] X.H. Wu, L.W. Yang, J.L. Yang, W.Y. Lin, Experimental study of linear motor direct-driven thermocompressor, AMR 732–733 (2013) 1147–1152, https://doi.org/10.4028/www.scientific.net/AMR.732-733.1147.
[29] Thomas, S. and Barth, E.J. (2019) Stirling Thermocompressor: Lumped Parameter Modeling and Experimental Impact of Displacer Motion Profile on Work Output, in *ASME/BATH 2019 Symposium on Fluid Power and Motion Control*, 07.10.2019 - 09.10.2019, Longboat Key, Florida, USA. American Society of Mechanical Engineers. doi: 10.1115/FPMC2019-1683.
[30] M. Beyer, Do you know the accuracy of your pressure sensor?: Find your way out of the waze of accuracy data? Sensor Magazin. (2008).
[31] Verein Deutscher Ingenieure (2013) *VDI-Wärmeatlas*, 11th edn, Springer Vieweg, Berlin, Heidelberg. 9783642199813.
[32] Fischer, F. and Kühl, H.-D. (2024) Experimental data for a three-stage overdriven free-displacer thermocompressor cascade (1.0) [Data Set]. doi: 10.5281/zenodo.10726185.